Lab on a Chip

Portable Light-sheet Optofluidic Microscopy for 3D Fluorescence Imaging Flow Cytometry

Journal:	*Lab on a Chip*
Manuscript ID	LC-ART-11-2022-001024.R1
Article Type:	Paper
Date Submitted by the Author:	08-Dec-2022
Complete List of Authors:	son, jeonghwan; Georgia Institute of Technology, Biomedical Engineering Mandracchia, Biagio; Georgia Institute of Technology, Biomedical Engineering; Emory University, Biomedical Engineering Silva Trenkle, Aaron ; Georgia Institute of Technology, Biomedical Engineering Kwong, Gabe; Georgia Institute of Technology, Biomedical Engineering Jia, Shu; Georgia Institute of Technology, Wallace H. Coulter Department of Biomedical Engineering

COMMUNICATION

Portable Light-sheet Optofluidic Microscopy for 3D Fluorescence Imaging Flow Cytometry

Jeonghwan Son,[a] Biagio Mandracchia,[a] Aaron D. Silva Trenkle,[a] Gabriel A. Kwong[ab] and Shu Jia[ab†]

Received 00th September 2022,
Accepted 00th September 2022

DOI: 10.1039/x0xx00000x

Imaging flow cytometry (IFC) combines conventional flow cytometry with optical microscopy, allowing for high-throughput, multi-parameter screening of single-cell specimens with morphological and spatial information. However, current 3D IFC systems are limited by instrumental complexity and incompatibility with available microfluidic devices or operations. Here, we report portable light-sheet optofluidic microscopy (PLSOM) for 3D fluorescence cytometric imaging. PLSOM exploits a compact, open-top light-sheet configuration compatible with commonly adopted microfluidic chips. The system offers a subcellular resolution (2-4 µm) in all three dimensions, high throughput (~1,000 cells/sec), and portability (30 cm (l) × 10 cm (w) × 26 cm (h)). We demonstrated PLSOM for 3D IFC using various phantom and cell systems. The low-cost and custom-built architecture of PLSOM permits easy adaptability and dissemination for broad 3D flow cytometric investigations.

Introduction

The advancement of optofluidics has allowed us to analyze and enumerate cellular properties across large populations with high throughput and multi-parameters[1-4]. In particular, imaging flow cytometry (IFC) marries flow cytometry and fluorescence microscopy, offering unprecedented spatial details, sensitivity and specificity of high-content biological specimens[5, 6]. Recent developments of IFC have further enhanced the resolution and throughput by implementing strategies such as camera functions[7], inertial focusing[8, 9], stroboscopic illumination[8-10], and virtual freezing[11]. However, these IFC techniques are primarily focused on 2D image data acquisition.

In contrast, the recent advances of 3D IFC have been reported to achieve the volumetric information of various biological specimens[12]. Amongst these efforts, light-sheet microscopy-based IFC has emerged as a promising approach with effective optical sectioning, low photobleaching, and high-resolution 3D reconstruction[13-17]. In particular, light-sheet microscopy utilizes a slice of light to illuminate the sample perpendicular to the direction of observation[18, 19]. The combination with microfluidics facilitates continuous light-sheet illumination on flowing objects in versatile formats such as refractive index-matching tubes[20], novel microchannels [21, 22], imaging capillaries[14, 17, 23] and microfluidic chips[13, 15, 24, 25], microfabricated optical elements[16], and engineered microfluidic chips[26]. However, the applicability of these major 3D IFC advances remains limited due to the complex implementation and less compatibility with general microfluidic devices and settings.

Meanwhile, open-top light-sheet microscopy has been proposed to locate all the optical components in an inverted fashion[27-32], thus enabling easy access to standard sample holders and imaging conditions. For instance, recent studies relying on the open-top light sheet have demonstrated mouse and Drosophila embryos in microfluidic conditions[29, 33]. However, such an open-top strategy remains unexplored for 3D flow cytometric single-cell study.

Here, we introduce PLSOM, a portable 3D IFC system based on the open-top light-sheet configuration for high-throughput single-cell investigation. PLSOM offers a compact, high-resolution IFC platform compatible with a wide range of microfluidic chips. In particular, the system provides subcellular resolution (2-4 µm) in all three dimensions, a high throughput (~1,000 cells/sec), and high portability (30 cm (l) × 10 cm (w) × 26 cm (h)). The low-cost optical elements and custom-built architecture permit easy adaptability and dissemination for broad flow cytometric studies.

Results

System design and experimental setup

---

[a] *Wallace H. Coulter Department of Biomedical Engineering, Georgia Institute of Technology and Emory University, Atlanta, GA 30332, USA*
[b] *Parker H. Petit Institute of Bioengineering and Bioscience, Georgia Institute of Technology, Atlanta, GA 30332, USA*
† Corresponding author: shu.jia@gatech.edu.

Electronic Supplementary Information (ESI) available. See DOI: 10.1039/x0xx00000x

The PLSOM system is illustrated in **Fig. 1(a, b)** and detailed in **Fig. S1**. The open-top light-sheet configuration contains perpendicular illumination and detection paths located underneath the sample holder. The flow speed in microfluidic channels is controlled by an external syringe pump (#55-2222, 28 cm (l) × 22.2 cm (w) × 14 cm (h), Harvard Apparatus). The illumination from a laser diode (LD, peak wavelength = 658 nm, L658P040, Thorlabs) and a power driver (#LDC 205C, 14.6 cm (l) × 6.6 cm (w) × 29 cm (h), Thorlabs) is collimated and propagated through a customized excitation filter (ET660/20m, Chroma) and an achromatic cylinder lens (CL, #68-160, NA 0.25, diameter = 12.5 mm, Edmund Optics). The CL generates a light sheet at the focal plane, where the sample inside the microfluidic channel is excited. The emitted fluorescence is collected by an aspheric plastic lens (OL, #66-001, NA 0.63, diameter = 25 mm, Edmund Optics), placed perpendicular to the illumination path, a customized emission filter (ET720/60m, Chroma), and a tube lens (L2). The images are recorded with a CMOS camera (GS3-U3-51S5M-C, camera pixel size = 3.45 µm, Edmund Optics) (**Fig. 1(a, b)**). The low-cost compact CL and OL, replacing conventional objective lenses, are mounted in customized chambers (**Fig. 1(c)**). The illumination path is oriented at an angle of 36° with respect to the horizontal microfluidic channel to accommodate the physical profiles and the focal lengths of the CL and OL (**Fig. 1(a)** and **Fig. S1**). A 3D-printed platform is accordingly used to adjust the entire setup by 9° to level the horizontal sample plane (**Fig. 1(b)**). The chamber was designed with SolidWorks and 3D-printed to contain the immersion water to reduce refractive index mismatch[29, 32], and secure the positions of the CL, OL, and microfluidic chips (**Fig. 1(c)**). The PLSOM setup exhibits a compact profile at 30 cm (l) × 10 cm (w) × 26 cm (h) and is weighted at 4 kg.

Data acquisition and processing

The PLSOM system acquires and processes data and reconstructs the volumetric information of objects following the pipeline as illustrated in **Fig. 1(d)**, **Fig. S3**, and **Supplementary Information**. The light-sheet illumination provides the optical sectioning capability, in which the thickness and Rayleigh range determine the effective plane of illumination of single-cell specimens[18] (**Fig. 1(d, left)**). Taking advantage of the fluidic motion, the system can acquire the plane of illumination that continuously sections the sample (**Fig. 1(d, middle)**). The reconstruction algorithm first addresses the mismatch between the flow speed and camera acquisition rate with the stacked images. We utilized 1D kymography from the acquired image stacks and identified the missing frames based on the centroid location of the sample in each image. After the interpolation of missing frames, the image stacks are then realigned to obtain the full volumetric reconstruction (**Fig. 1(d, right)** and **Fig. S3**). Finally, we processed the 3D images using deconvolution to enhance the resolution and image quality (**Supplementary Note 2**).

System characterization

To characterize the performance of PLSOM, we first measured the magnification of the system using a laser diode (PL450B, 450

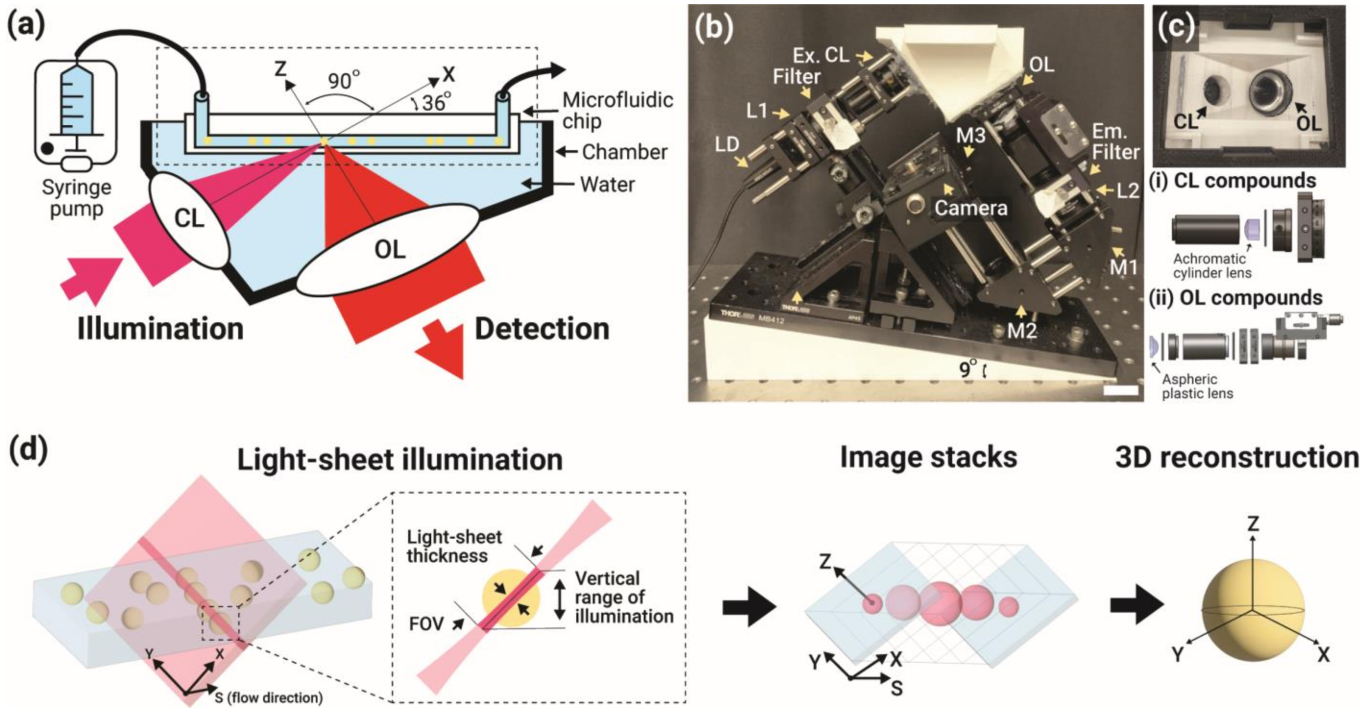

Figure 1. Portable light-sheet optofluidic microscopy (PLSOM) for 3D Imaging Flow Cytometry. (a) Schematic of the PLSOM setup. The open-top configuration places the system underneath the microfluidic chip. The cylinder lens (CL) forms the thin light-sheet illumination at an angle of 36° with respect to the horizontal sample plane, and the objective lens (OL) collects the emitted light at the focal plane perpendicular to the axis of illumination. Both CL and OL are immersed in water to reduce the mismatch of refractive indices. (b) Photograph of the system. The details are illustrated in the Supplementary Information. LD, laser diode; L, lens; M, mirror; Ex, excitation; Em, emission. (c) Customized water-immersion chamber for the CL, OL, and sample holder. Insets (i, ii) show the CL and OL compounds (see Supplementary Information). (d) Data acquisition, kymography processing, and 3D reconstruction of PLSOM. Scale bar: 25 mm (b).

nm wavelength, Thorlabs) and a customized excitation filter (ET450/30×, Chroma). We imaged a water-immersed negative USAF target (R1DS1N, Thorlabs), and based on the known physical distance, we derived the magnification (14.5×) and effective pixel size (240 nm) of the system (**Fig. 2(a-c)**).

We then used a reflective mirror with a customized holder compensating for the tilted optical axis (9°) to measure the thickness of the light sheet (3.79 µm) (**Fig. 2(d, e)**) at the peak wavelength of 658 nm. The thickness of the light sheet determines the optical sectioning capability of the system. Here, PLSOM offers slightly lower optical sectioning in comparison with the theoretical prediction[18] (3.2 µm), mainly due to the residual aberrations caused by the use of the plastic lens. We also verified the FOV of the PLSOM system at 490 µm × 25 µm using the full camera sensor (8.5 mm × 7.1 mm) and the effective vertical range of illumination (25 µm × sine (36°) = 14.5 µm) (**Fig. 1(d, left)**).

Next, we implemented microfluidic chips with 500 µm (width) × 30 µm (depth) channels (10001824, clear glass lid thickness = 170 µm, Microfluidic ChipShop GmbH). An experimental throughput (~1,000 cells/sec) was measured by counting HeLa cells labelled with the plasma membrane throughout the entire FOV in the microfluidic channel at an average flow speed of 207.9 µm/sec, (**Fig. 2(f, g)**). Notably, the flow speed was limited by the number of frames needed to acquire the entire sample volume, **Fig. S2**. With the light-sheet thickness of ~4 µm, we reason that at least three frames are needed to seamlessly scan the diameter of a cell (10-15 µm). As a result, the flow speed can be theoretically predicted at 206 µm/sec with the frame rate at 60 Hz, resulting in the analytical throughput (1,180 cells/sec at the 80% cell density in the channel with the cell diameter of 10 µm), consistent with the experimental measurement. In this work, we chose to use various flow rates below this limit to facilitate sufficient light-sheet sectioning for reconstruction. The potential interference of the light sheet and the microfluidic channel can be controlled by locating the microfluidic chip on a proper focal plane.

Lastly, we imaged 200-nm fluorescent beads (T7280, TetraSpek, Invitrogen) on a glass slide and cover slide (thickness = 170 µm) and recorded the point-spread function (PSF) of the system by mechanically scanning the sample stage at a 1-µm step size along the flow direction (**Fig. 2(h-j)**). With the reconstruction process as shown in **Fig. S3** and **Supplementary Information**, the 3D PSF images were Gaussian-fitted, showing the full width at half maximum (FWHM) values at 2.9 µm laterally and 3.43 µm axially (**Fig. 2(i, j)**). The axial measurement indicates a good agreement with the thickness of the light sheet (3.79 µm in **Fig. 2(e)**).

PLSOM imaging of phantom and HeLa cells

To validate the performance of PLSOM, we first imaged and reconstructed flowing phantom samples that contain two mixed types of fluorescent beads (7 µm, FSFR007, Bangs Laboratories; 15 µm, F7238, Invitrogen) (**Fig. 3(a-g)**). The measurements of the reconstructed objects yielded two distinct populations, in which both the intensity and 3D volume are consistent with the known physical sizes and the 2D measurement of the samples (**Fig. 3(h, i)**). Next, using PLSOM, we imaged the plasma membrane of HeLa cells circulating at the flow speed of 111.39 µm/sec (**Fig. 3 (j-p)**). The 3D imaging capability exhibited effective optical sectioning that allows for the synthesis of the focal stacks of the entire objects, showing the native, sphere-like morphology of cells in the flow (**Fig. 3 (j-m)**). The 3D reconstructed images display a consistent cell size (radius at ~5 µm, **Fig. 3 (n,o)**) in all three dimensions, in agreement with the volumetric measurement (mean volume = 955.5 μm^3, **Fig. 3 (p)**), as well as consistent with the known 10-15 µm HeLa cell size in the flow[34].

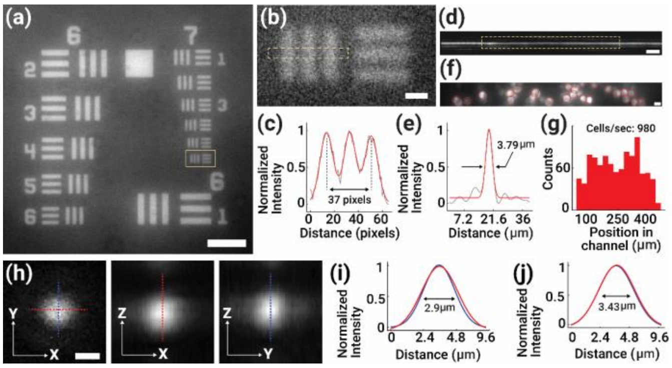

Figure 2. System characterization. (a) Selected region of the bright-field image of a USAF target taken by PLSOM. (b) Zoomed-in image of the boxed region in (a). (c) Cross-sectional intensity profile of the boxed region in (b). The three bars span 37 pixels, corresponding to 14.5× magnification and 240-nm effective pixel size, based on the known physical size of the caliber sample (4.4 µm between adjacent bars). (d) Image of the mirror-reflected light sheet at the focal plane of illumination. (e) Cross-sectional intensity profile of the boxed region in (d), displaying the FWHM value of 3.79 µm. (f) Raw light-sheet image of HeLa cells stained and segmented for the plasma membrane in the microfluidic channel. (g) Histogram of cell counts across the FOV yields the experimental throughput of the system at ~1,000 cells/sec at the average flow speed of 207.9 µm/sec. (h) Reconstructed PSF images of a 200-nm fluorescent bead in x-y, x-z, and y-z dimensions. (i,j) Cross-sectional profiles across the dashed lines in (h) of the PSF in x-y (i) and z (j), exhibiting the FWHM values of 2.9 µm and 3.43 µm, respectively. Scale bars: 50 µm (a), 5 µm (b), 30 µm (d), 15 µm (f), 3 µm (h).

Imaging human T cells and Jurkat cells

Next, we examined PLSOM by imaging mixed human T cells (hT) and Jurkat cells (JK) both stained for the plasma membrane in the microfluidic channel. The system recorded and reconstructed the sequential focal stacks of the cells flowing through the light sheet (**Fig. 4(a)**). Compared to conventional 2D methods, the 3D reconstructed images allow us to differentiate the hT and JK cells based on the volumetric rendering of the samples (**Fig. 4(b-g)**). The images also showed a consistent measurement of the membrane stain (~3 µm) that agrees with the PSF of PLSOM using the caliber samples (**Fig. 2(i, j)**). The total fluorescence intensity originating from the 3D reconstructed volume showed a linear relationship as a function of the volume, where the slope is determined by the fluorophore labelling density (**Fig. 4(h)**).

Furthermore, the size histogram measured using the reconstructed 2D focal stacks displayed two distinct groups of cells (**Fig. 4(i)**). The two distinct maxima show the mean diameters of hT cells (7.4 µm) and JK cells (11.7 µm) in the

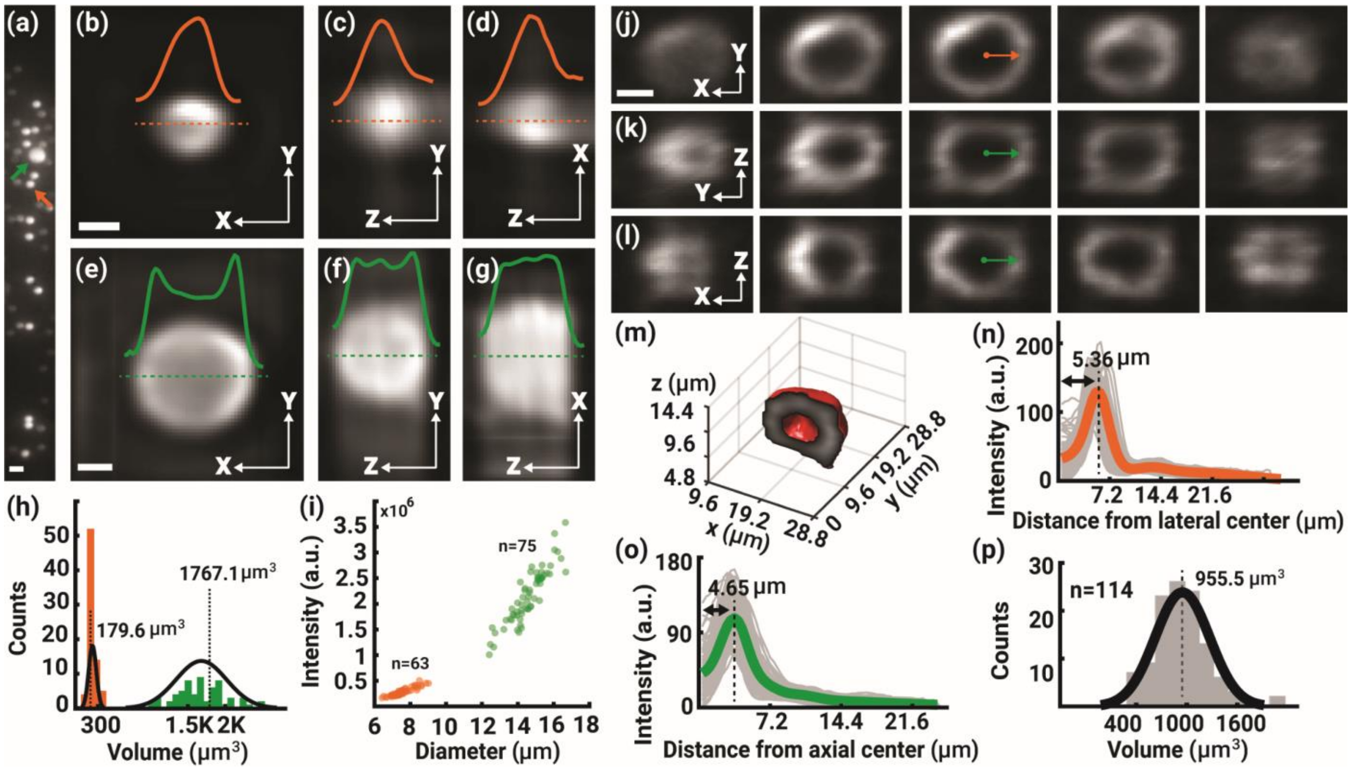

Figure 3. PLSOM imaging of microspheres and HeLa cells. (a) Raw light-sheet image of mixed fluorescent microspheres (7 μm, orange arrow; 15 μm, green arrow) flowing through the microfluidic channel. (b-d) 3D reconstructed images of a 7-μm throughout-labelled bead at an average flow speed of 181.5 μm/sec in x-y (b, focal stack image), y-z (c, maximum intensity projection, or MIP), and x-z (d, MIP). The insets show the corresponding cross-sectional intensity profiles along the orange dashed lines. (e-g) 3D reconstructed images of a 15-μm surface-labelled bead at an average flow speed of 133.8 μm/sec in x-y (e, focal stack image), y-z (f, MIP), and x-z (g, MIP). The insets show the corresponding cross-sectional intensity profiles along the green dashed lines. (h) Histogram counts of the 3D reconstructed volumes, differentiating two distinct populations of microspheres with maxima at 224.4 ± 49.6 μm^3 and 1650.4 ± 330.6 μm^3. The dashed lines indicate the volume values (179.6 μm^3 and 1767.1 μm^3) derived based on the respective physical sizes of 7 μm and 15 μm. (i) Scatter plot of the total volumetric fluorescent intensity of the microsphere mixture as a function of the diameter as rendered from the experimental volume measurement in (h). (j-l) 3D reconstructed images of a membrane-labelled HeLa cell at an average flow speed of 111.4 μm/sec shown in x-y (j), y-z (k), x-z (l) stacks (step size = 2.4 μm). (m) 3D reconstructed volume of the cell in (j-l), where the hollow cellular structure was clearly observed. (n,o) Radial profiles (gray) of the cross-sectional intensity, as indicated by the arrows in (j-l), of the cell population in the lateral (n) and axial (o) dimensions, exhibiting the mean radii of 5.36 μm and 4.65 μm, respectively. (p) Histogram of cell volumes, showing the mean volume at 955.5 ± 322.8 μm^3 of HeLa cells. Scale bars: 15 μm (a), 5 μm (b, e, j).

lateral plane, consistent with the previously reported diameters of hT[35] (8 μm) and Jurkat cells[9, 36] (11.5 μm). Also, the results agree with the same measurement from the pure population of hT cells (mean = 6.9 μm) and the measurement of the radial maxima using the raw 2D light-sheet datasets (8.1 μm and 12.3 μm, **Fig. 4(i)**, dashed lines). Notably, the 3D imaging capability of PLSOM allows us to directly quantify the volumes of the two cell types, each with a mean value of 108 μm^3 (hT) and 675 μm^3 (JK) (**Fig. 4(j)**). Volumetric imaging effectively considers the varying 3D morphology of cells, leading to more accurate cellular quantification in comparison with the values derived using the conventional measurement from the raw 2D images in the lateral plane while assuming the cell morphology as a sphere (280 μm^3 and 970 μm^3, respectively) (**Fig. 4(j)**, dashed lines).

PLSOM imaging of drug-administered HeLa cells

Lastly, we administered live HeLa cells with paclitaxel (Taxol), a chemotherapy drug that can destabilize the formation of cytoskeletons and induce apoptosis by blocking cell cycles[37, 38]. In this experiment, 400 nM of Taxol was used for 8 hours of administration of live HeLa cells. Using PLSOM, we performed cytometric imaging of the mixture of untreated and treated cells stained for both the plasma membrane (Cell Mask Deep Red) and the nucleus (SYTOX Deep Red). As observed, this cytotoxicity assay allows us to label the membrane of both cell groups while only the nuclei of those drug-affected cells that possess compromised plasma membrane (**Fig. 5(a-c)**). Compared to conventional 2D images that lack optical sectioning and may thus confuse the emitted fluorescence from the membrane and nucleus, PLSOM offers the 3D reconstructed focal stacks that clearly differentiate the two cytotoxic states of the cells (**Fig. 5(b, c)**). Quantifying the cell morphology, we observed that the treated cells exhibited an enlarged volume in all three dimensions than the untreated group, primarily due to Taxol-induced cell swelling in the process of cell death[39] (**Fig. 5(d-g)**). Using the 3D datasets, we also segmented the cellular features and determined the volumetric ratio between the fluorescence emitted from the nucleus and the plasma membrane (**Fig. 5(h)** and **Fig. S3**). It is clearly shown that the cells unaffected or less affected by the drug remained at both a relatively small volume (no cell swelling) and a low ratio (no nuclei labels), while the drug-affect group exhibited the linearly-correlated increase in both the cell volume and the fluorescence from the nuclei (**Fig. 5(i)**). Furthermore, the principal components analysis (PCA, MATLAB) of the datasets reveals two distinctive patterns, identifying the drug-induced effect of the

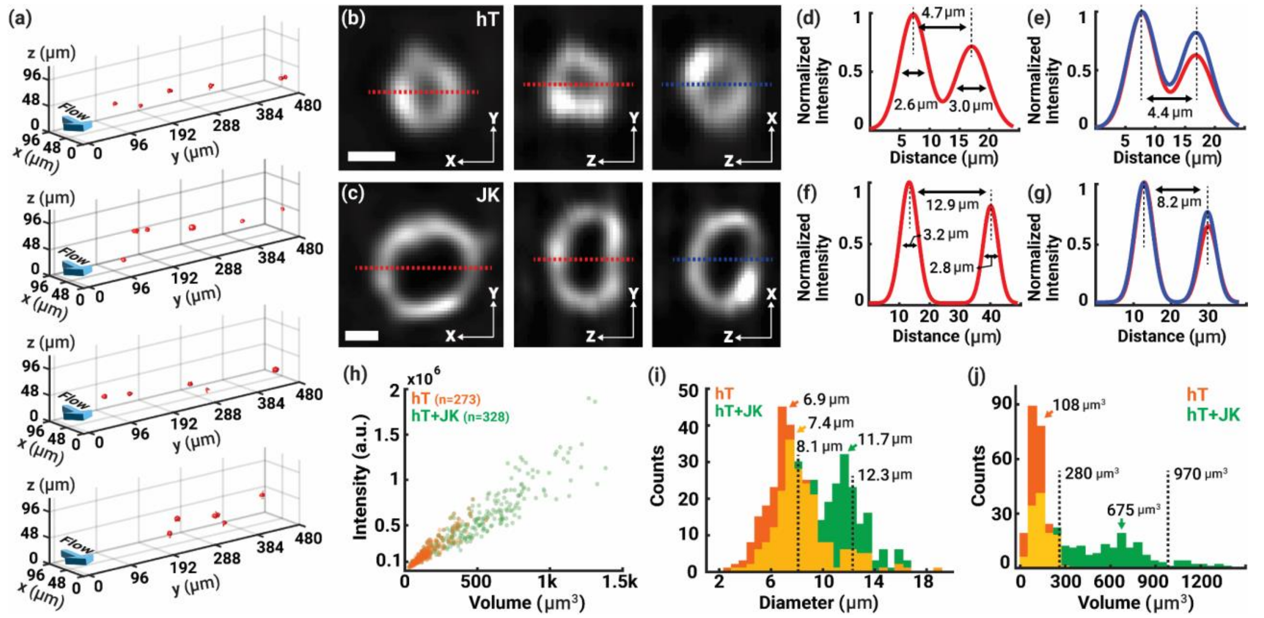

Figure 4. PLSOM imaging of human T (hT) cells and Jurkat (JK) cells. (a) Four examples of 3D reconstructed mixed populations of cells in the flow. (b, c) 3D reconstructed membrane-labelled hT cells (b) and JK cells (c) in x-y, y-z, and x-z cross-sectional views. (d-g) Cross-sectional intensity profiles in x (d,f) and z (e,g) dimensions of hT cells (d,e) at an average flow speed of 54.5 μm/sec and JK cells (f,g) at an average flow speed of 147.2 μm/sec. (h) Scatter plot of the fluorescence intensity as a function of the cell volume. (i) Histogram counts of the cell diameters for the pure hT cell population (red, 6.9 μm) and the mixed populations (green, 7.4 μm and 11.7 μm) measured from the reconstructed focal stacks. Yellow bars denote the overlap of the two (red and green) distributions. The dashed lines indicate the size measurement of the two cell groups using the raw 2D datasets (8.1 μm and 12.3 μm). (j) Histogram counts of the corresponding cell volumes, showing more accurate 3D measurements compared to the 2D results of the raw datasets (dashed lines). Scale bars: 5 μm (b, c).

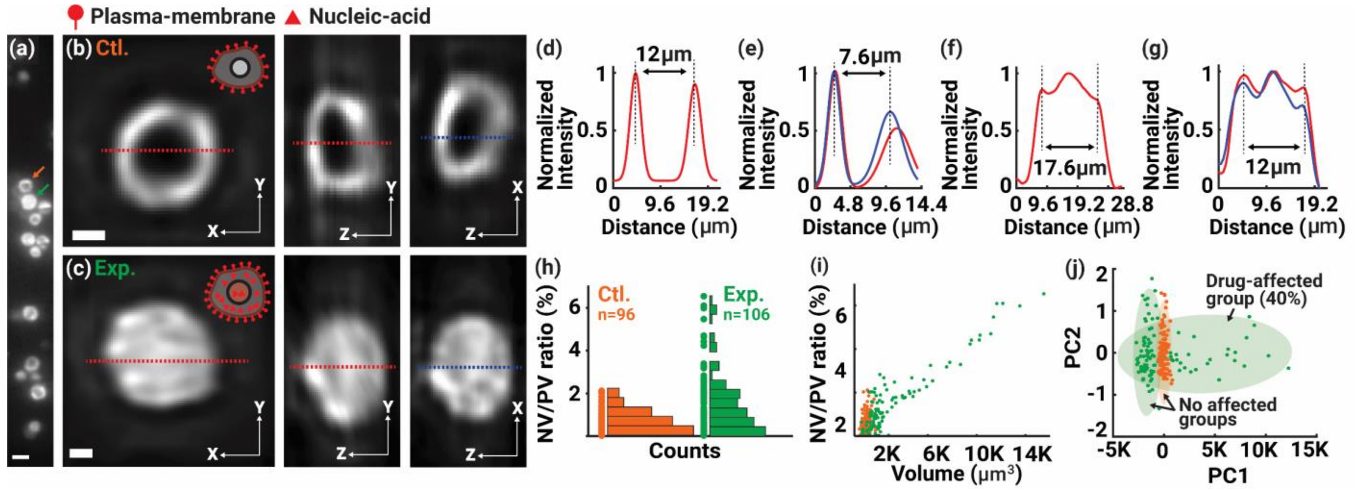

Figure 5. PLSOM imaging of drug-administered HeLa cells. (a) Raw light-sheet image of the mixture of untreated (control) and Taxol-treated (experimental) HeLa cells. The orange arrow points to a cell with only the plasma membrane stained. The green arrow points to a cell with both the membrane and nucleus stained. (b, c) Cross-sectional images of the control and drug-affected cells in x-y, y-z, and x-z. (d-g) Corresponding cross-sectional intensity profiles of the control (d,e) at an average flow speed of 47 μm/sec and drug-affected (f,g) cells at an average flow speed of 65.8 μm/sec in the lateral (d,f) and axial (e,g) dimensions. (h) histogram counts of the fluorescence intensity ratio between the nucleus (NV) and the plasma membrane (PV). (i) The ratio as in (h) as a function of the cell volume, showing two main distributions of the control (low ratios and volumes) and drug-affected (linearly increased ratio and volumes) cells. (j) Principal components analysis (PCA) of the datasets, displaying two distinctive patterns of the unaffected cells and the ~40% drug-affected cells among the experimental group. The elliptical shadows denote 95% of the standard deviations in each group. Scale bars: 20 μm (a), 5 μm (b, c).

cytotoxic cell population and indicating an efficacy rate of about 40% (**Fig. 5(j)**).

Conclusions

We have developed the portable light-sheet optofluidic microscopy system, PLSOM, for 3D flow cytometric imaging. The system exploits the advantage of the compact, open-top configuration (30 cm × 10 cm × 26 cm) for easy accessibility to commonly adopted microfluidic and imaging settings. The portability of the imaging system also allows for high compatibility with diverse fluidic and illumination systems. The light-sheet illumination allows for the simultaneous acquisition of single-cell specimens across the entire imaging field of view (490 μm × 25 μm), yielding a high throughput at ~1,000 cells/sec at a 60-Hz acquisition rate. The 3D imaging capability and resolution (~3 μm laterally and ~4 μm axially) of PLSOM reveal the volumetric subcellular details of cells, enabling a wide range of structural and functional assays for enumerating and interrogating single-cell populations. The performance of PLSOM can be further enhanced by implementing both hardware and software developments such as faster sensors, multi-color excitation, stroboscopic illumination, and advanced image processing algorithms. Diverse approaches could be applicable in the PLSOM system for strategic multi-color implementation on detection[9, 33, 40-42] and illumination, such as mitigating chromatic aberrations by an optimized cylindrical lens[43, 44], combination with a spherical mirror[45], beam engineering[46], separate relay lenses, or achromatic objective lens. In addition, the implementation of recent deep-learning-based algorithms could allow the PLSOM system for rapid and automated screening of samples[47]. We anticipate the portable system as a promising tool for various 3D flow cytometric applications in basic biological research and point-of-care clinical diagnostics.

Author Contributions

J.S., B.M., and S.J. conceived and designed the project. J.S. constructed the system, developed the algorithm, and conducted experiments and data analysis. B.M. helped with system design and image processing. A.D.S.T. and G.A.K. helped with the human T cell samples. S.J. supervised the project. J.S. and S.J. wrote the manuscript.

Conflicts of interest

G.A.K. is co-founder and equity shareholder of Glympse Bio and Port Therapeutics. This study could affect his personal financial status. The terms of this arrangement have been reviewed and approved by Georgia Tech in accordance with its conflict-of-interest policies.

Acknowledgments

We acknowledge the support of the faculty start-up fund of Georgia Institute of Technology (S.J.), NIH grant R35GM124846 (S.J.), NSF grants EFMA1830941 and DBI2145235 (S.J.), NSF Graduate Research Fellowships Program DGE-2039655 (A.D.S.T.), and NIH Cell and Tissue Engineering (CTEng) Training Program T32GM145735 (A.D.S.T.)

Notes and references

1. N. T. Huang, H. L. Zhang, M. T. Chung, J. H. Seo and K. Kurabayashi, *Lab Chip*, 2014, **14**, 1230-1245.
2. X. Fan and I. M. White, *Nature Photonics*, 2011, **5**, 591-597.
3. D. Psaltis, S. R. Quake and C. Yang, *Nature*, 2006, **442**, 381-386.
4. P. Minzioni, R. Osellame, C. Sada, S. Zhao, F. G. Omenetto, K. B. Gylfason, T. Haraldsson, Y. B. Zhang, A. Ozcan, A. Wax, F. Mugele, H. Schmidt, G. Testa, R. Bernini, J. Guck, C. Liberale, K. Berg-Sorensen, J. Chen, M. Pollnau, S. Xiong, A. Q. Liu, C. C. Shiue, S. K. Fan, D. Erickson and D. Sinton, *Journal of Optics*, 2017, **19**, 093003.
5. Y. Han, Y. Gu, A. C. Zhang and Y. H. Lo, *Lab Chip*, 2016, **16**, 4639-4647.
6. B. K. McFarlin and M. A. Gary, *Methods*, 2017, **112**, 1-8.
7. E. D. Diebold, B. Buckley, D. R. Gossett and B. Jalali, *Nature Photonics*, 2013, **7**, 806-810.
8. A. S. Rane, J. Rutkauskaite, A. deMello and S. Stavrakis, *Chem*, 2017, **3**, 588-602.
9. G. Holzner, B. Mateescu, D. van Leeuwen, G. Cereghetti, R. Dechant, S. Stavrakis and A. deMello, *Cell Reports*, 2021, **34**, 108824.
10. T. Miura, H. Mikami, A. Isozaki, T. Ito, Y. Ozeki and K. Goda, *Biomedical Optics Express*, 2018, **9**, 3424-3424.
11. H. Mikami, M. Kawaguchi, C. J. Huang, H. Matsumura, T. Sugimura, K. Huang, C. Lei, S. Ueno, T. Miura, T. Ito, K. Nagasawa, T. Maeno, H. Watarai, M. Yamagishi, S. Uemura, S. Ohnuki, Y. Ohya, H. Kurokawa, S. Matsusaka, C. W. Sun, Y. Ozeki and K. Goda, *Nat Commun*, 2020, **11**, 1162.
12. E. J. Gualda, H. Pereira, G. G. Martins, R. Gardner and N. Moreno, *Cytometry Part A*, 2017, **91a**, 144-151.
13. R. Regmi, K. Mohan and P. P. Mondal, *AIP Advances*, 2014, **4**, 097125.
14. M. Ugawa and S. Ota, *Small Science*, 2022, **2**, 2100126.
15. P. Kumar, P. Joshi, J. Basumatary and P. P. Mondal, *Sci Rep*, 2022, **12**, 78.
16. E. J. Vargas-Ordaz, S. Gorelick, H. M. York, B. Liu, M. L. Halls, S. Arumugam, A. Neild, A. de Marco and V. J. Cadarso, *Lab on a Chip*, 2021, **21**, 2945-2954.
17. M. Ugawa and S. Ota, *Biomed Opt Express*, 2022, **13**, 3647-3656.
18. O. E. Olarte, J. Andilla, E. J. Gualda and P. Loza-Alvarez, *Advances in Optics and Photonics*, 2018, **10**, 111-179.
19. J. M. Girkin and M. T. Carvalho, *Journal of Optics*, 2018, **20**, 053002.
20. E. J. Gualda, H. Pereira, T. Vale, M. F. Estrada, C. Brito and N. Moreno, *Biomed Opt Express*, 2015, **6**, 4447-4456.
21. P. Paiè, F. Bragheri, A. Bassi and R. Osellame, *Lab on a Chip*, 2016, **16**, 1556-1560.
22. F. Sala, M. Castriotta, P. Paie, A. Farina, S. D'Annunzio, A. Zippo, R. Osellame, F. Bragheri and A. Bassi, *Biomed Opt Express*, 2020, **11**, 4397-4407.
23. J. Wu, J. Li and R. K. Chan, *Opt Express*, 2013, **21**, 14474-14480.
24. H. Jiang, T. Zhu, H. Zhang, J. Nie, Z. Guan, C. M. Ho, S. Liu and P. Fei, *Lab Chip*, 2017, **17**, 2193-2197.
25. R. Regmi, K. Mohan and P. P. Mondal, *Microsc Res Tech*, 2013, **76**, 1101-1107.
26. Y.-J. Fan, H.-Y. Hsieh, S.-F. Tsai, C.-H. Wu, C.-M. Lee, Y.-T. Liu, C.-H. Lu, S.-W. Chang and B.-C. Chen, *Lab on a Chip*, 2021, **21**, 344-354.
27. A. K. Glaser, N. P. Reder, Y. Chen, C. Yin, L. Wei, S. Kang, L. A. Barner, W. Xie, E. F. McCarty and C. Mao, *Nature communications*, 2019, **10**, 1-8.
28. L. A. Barner, A. K. Glaser, H. Huang, L. D. True and J. T. Liu, *Biomedical Optics Express*, 2020, **11**, 6605-6619.
29. R. McGorty, H. Liu, D. Kamiyama, Z. Dong, S. Guo and B. Huang, *Optics express*, 2015, **23**, 16142-16153.
30. S. Bakas, D. Uttamchandani, H. Toshiyoshi and R. Bauer, *Scientific reports*, 2021, **11**, 1-11.

31. L. A. Barner, A. K. Glaser, L. D. True, N. P. Reder and J. T. Liu, *Optics letters*, 2019, **44**, 4451-4454.
32. B. Kim, M. Na, S. Park, K. Kim, J.-H. Park, E. Chung, S. Chang and K. H. Kim, *Biomedical Optics Express*, 2021, **12**, 2328-2338.
33. P. Strnad, S. Gunther, J. Reichmann, U. Krzic, B. Balazs, G. De Medeiros, N. Norlin, T. Hiiragi, L. Hufnagel and J. Ellenberg, *Nature methods*, 2016, **13**, 139-142.
34. M. B. James and T. D. Giorgio, *Molecular Therapy*, 2000, **1**, 339-346.
35. A. D. Stern, A. H. Rahman and M. R. Birtwistle, *Cytometry A*, 2017, **91**, 14-24.
36. M. J. Rosenbluth, W. A. Lam and D. A. Fletcher, *Biophys J*, 2006, **90**, 2994-3003.
37. A. Mielgo, V. A. Torres, K. Clair, S. Barbero and D. G. Stupack, *Oncogene*, 2009, **28**, 3551-3562.
38. P. De, J. H. Carlson, B. Leyland-Jones, C. Williams and N. Dey, *Sci Rep*, 2018, **8**, 13192.
39. X.-P. Wang, T.-S. Chen, L. Sun, J.-Y. Cai, M.-Q. Wu and M. Mok, *Micron*, 2008, **39**, 1216-1221.
40. P. Rosendahl, K. Plak, A. Jacobi, M. Kraeter, N. Toepfner, O. Otto, C. Herold, M. Winzi, M. Herbig and Y. Ge, *Nature methods*, 2018, **15**, 355-358.
41. V. Voleti, K. B. Patel, W. Li, C. Perez Campos, S. Bharadwaj, H. Yu, C. Ford, M. J. Casper, R. W. Yan and W. Liang, *Nature methods*, 2019, **16**, 1054-1062.
42. H. Mikami, M. Kawaguchi, C.-J. Huang, H. Matsumura, T. Sugimura, K. Huang, C. Lei, S. Ueno, T. Miura and T. Ito, *Nature communications*, 2020, **11**, 1-11.
43. J. Licea-Rodriguez, A. Figueroa-Melendez, K. Falaggis, M. P. Sánchez, M. Riquelme and I. Rocha-Mendoza, *Journal of biomedical optics*, 2019, **24**, 016501.
44. K. Greger, J. Swoger and E. Stelzer, *Review of Scientific Instruments*, 2007, **78**, 023705.
45. T. Bruns, M. Bauer, S. Bruns, H. Meyer, D. Kubin and H. Schneckenburger, *Journal of Microscopy*, 2016, **264**, 261-267.
46. Y. Y. Luna‐Palacios, J. Licea‐Rodriguez, M. D. Camacho‐Lopez, I. Teichert, M. Riquelme and I. Rocha‐Mendoza, *Journal of Biophotonics*, 2022, e202100359.
47. Z. Göröcs, D. Baum, F. Song, K. de Haan, H. C. Koydemir, Y. Qiu, Z. Cai, T. Skandakumar, S. Peterman and M. Tamamitsu, *Lab on a Chip*, 2020, **20**, 4404-4412.